



Cite as
Nano-Micro Lett.
(2024) 16:195

Received: 17 January 2024
Accepted: 15 March 2024
© The Author(s) 2024

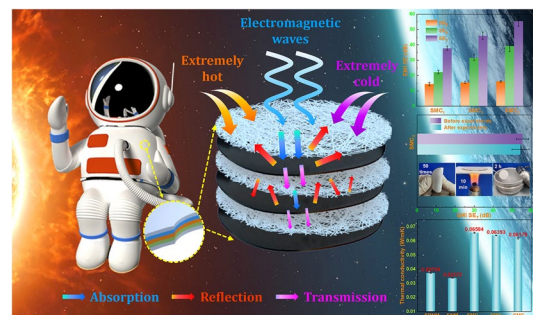
MXene@c-MWCNT Adhesive Silica Nanofiber Membranes Enhancing Electromagnetic Interference Shielding and Thermal Insulation Performance in Extreme Environments

Ziyuan Han¹, Yutao Niu^{2,3}, Xuetao Shi⁴, Duo Pan¹ ✉, Hu Liu¹ ✉, Hua Qiu⁴, Weihua Chen^{1,5}, Ben Bin Xu⁶, Zeinhom M. El-Bahy⁷, Hua Hou⁶, Eman Ramadan Elsharkawy⁸, Mohammed A. Amin⁹, Chuntai Liu¹, Zhanhu Guo⁶

HIGHLIGHTS

- The SiO₂ nanofiber membranes and MXene@c-MWCNT_{6,4} as one unit layer (SMC₁) were bonded together with 5 wt% PVA solution.
- When the structural unit is increased to three layers, the resulting SMC₃ has an average electromagnetic interference SE_T of 55.4 dB and a low thermal conductivity of 0.062 W m⁻¹ K⁻¹.
- SMC_x exhibit stable electromagnetic interference shielding and excellent thermal insulation even in extreme heat and cold environment.

ABSTRACT A lightweight flexible thermally stable composite is fabricated by combining silica nanofiber membranes (SNM) with MXene@c-MWCNT hybrid film. The flexible SNM with outstanding thermal insulation are prepared from tetraethyl orthosilicate hydrolysis and condensation by electrospinning and high-temperature calcination; the MXene@c-MWCNT_{x,y} films are prepared by vacuum filtration technology. In particular, the SNM and MXene@c-MWCNT_{6,4} as one unit layer (SMC₁) are bonded together with 5 wt% polyvinyl alcohol (PVA) solution, which exhibits low thermal conductivity (0.066 W m⁻¹ K⁻¹) and good electromagnetic interference (EMI) shielding performance (average EMI SE_T, 37.8 dB). With the increase in functional unit layer, the overall thermal insulation performance of the whole composite film (SMC_x) remains stable, and EMI shielding performance is greatly improved, especially for SMC₃ with three unit layers, the average EMI SE_T is as high as 55.4 dB. In addition, the organic combination of rigid SNM and tough MXene@c-MWCNT_{6,4} makes SMC_x exhibit good mechanical tensile strength. Importantly, SMC_x exhibit stable EMI shielding and excellent thermal insulation even in extreme heat and cold environment. Therefore, this work provides a novel design idea and important reference value for EMI shielding and thermal insulation components used in extreme environmental protection equipment in the future.



KEYWORDS SiO₂ nanofiber membranes; MXene@c-MWCNT; Composite film; Thermal insulation; Electromagnetic interference shielding

✉ Duo Pan, panduonerc@zzu.edu.cn; Hu Liu, liuhu@zzu.edu.cn

¹ Key Laboratory of Materials Processing and Mold (Zhengzhou University), Ministry of Education, National Engineering Research Center for Advanced Polymer Processing Technology, Zhengzhou University, Zhengzhou 450002, People's Republic of China

² School of Nano-Tech and Nano-Bionics, University of Science and Technology of China, Hefei 230026, People's Republic of China

³ Key Laboratory of Multifunctional Nanomaterials and Smart Systems, Advanced Materials Division, Suzhou Institute of Nano-Tech and Nano-Bionics, Chinese Academy of Sciences, Suzhou 215123, People's Republic of China

⁴ Shaanxi Key Laboratory of Macromolecular Science and Technology, School of Chemistry and Chemical Engineering, Northwestern Polytechnical University, Xi'an 710072, People's Republic of China

⁵ College of Chemistry & Green Catalysis Center, Zhengzhou University, Zhengzhou 450001, People's Republic of China

⁶ Mechanical and Construction Engineering, Faculty of Engineering and Environment, Northumbria University, Newcastle Upon Tyne NE1 8, UK

⁷ Department of Chemistry, Faculty of Science, Al-Azhar University, Nasr City 11884, Cairo, Egypt

⁸ Department of Chemistry, Faculty of Science, Northern Border University, Arar, Saudi Arabia

⁹ Department of Chemistry, College of Science, Taif University, P.O. Box 11099, 21944 Taif, Saudi Arabia

Published online: 14 May 2024



SHANGHAI JIAO TONG UNIVERSITY PRESS

Springer

1 Introduction

In recent years, manned spaceflight has become an important symbol to measure a country's scientific and technological strength. In the face of the extreme environment of space with large temperature difference, strong radiation and high vacuum, the extra-vehicular space suit has become the necessary protective equipment for astronauts to go outside the space station and carry out various kinds of work [1, 2]. For a complete space suit, the previous thermal control system and radiation protection system are relatively independent, and the design materials are complex and heavy, which seriously restrict the physical mobility of astronauts. Therefore, the development of lightweight, flexible, low-cost materials with both electromagnetic interference (EMI) shielding and thermal insulation is the key to ensure the normal life and work of astronauts in space [3, 4].

Conventional thermal insulation materials are mainly divided into foam-based materials [5], phase change materials [6] and ceramic aerogel materials [7]. Among them, foam-based thermal insulation materials have defects such as low ignition point and release of toxic substances during combustion. For most phase change insulation materials, maintaining long-lasting insulation performance requires a large space volume due to fixed enthalpy values. Ceramic aerogel materials have low thermal conductivity and slow phonon transfer rate; especially for silica (SiO_2) aerogel, it has small pore size, high porosity and thermal stability, so it is a lightweight and efficient thermal insulation material [8, 9]. However, in practical applications, researchers found that SiO_2 aerogel is highly transparent to infrared radiation and has great brittleness [10]. With the development of nanotechnology in recent years, effective progress has been made in converting SiO_2 sol into flexible SiO_2 nanofiber membranes (SNM), and the obtained SNM shows excellent heat insulation and good thermal stability based on its special pore structure [11, 12]. Si et al. [13] successfully synthesized ultra-softness SNM, which not only have excellent tensile strength of 5.5 MPa, but also exhibit ultra-low thermal conductivity of $0.0058 \text{ W m}^{-1} \text{ K}^{-1}$. Currently, the ways to obtain SNM include laser ablation [14], sol-gel [15], vapor deposition [16] and electrospinning [17]. Compared with other methods, electrospinning has the advantages of simple operation, low cost and good controllability [18–20].

In terms of EMI shielding, MXene, a two-dimensional structural material with high electrical conductivity, has been widely studied [21–23]. However, poor mechanical,

chemical and thermal stability greatly limits its application range [24]. Carbon nanotube (CNT) has high aspect ratio, low density, outstanding mechanical properties, high electrical conductivity, and good chemical stability [25–27]; therefore, it is another ideal EMI shielding conductive filler; unfortunately, weak dispersion has always been a problem [28]. It has been found that the combination of MXene and CNT by special means can not only overcome the defects of each other, but also make the hybrid fillers have good comprehensive properties [29]. For example, Zhou et al. [30] combined MXene and CNT uniformly through vacuum-assisted filtration and demonstrated good EMI shielding performance and high tensile strength and toughness in the obtained MXene/CNT films. In fact, conductive fillers such as MXene and CNT have considerable thermal conductivity [31–33], so how to combine them with thermal insulation materials and coordinate EMI shielding and thermal insulation performance is always a challenge in the design of aerospace protective suits.

In this work, SiO_2 nanofiber membranes (SNM), which mainly play an EMI shielding function, were successfully prepared by electrospinning of tetraethyl orthosilicate hydrolyzed precursor followed with a high-temperature calcination condensation process. As a component of EMI shielding function, MXene@c-MWCNT_{x:y} is obtained through vacuum filtration with MXene/c-MWCNT of different hybrid ratios, and it is found that when the mass ratio of MXene to c-MWCNT is 6:4, MXene@c-MWCNT_{6:4} has the optimal mechanical and functional properties. Then, SNM and MXene@c-MWCNT_{6:4} are effectively formed into an organic whole by cleverly using 5 wt% polyvinyl alcohol (PVA) as a binder, and this structural unit (SNM/MXene@c-MWCNT_{6:4}, SMC₁) exhibits excellent EMI shielding and heat insulation properties. When the structural unit is increased to three layers, the resulting SMC₃ has an average EMI SE_T of 55.4 dB and a low thermal conductivity of $0.062 \text{ W m}^{-1} \text{ K}^{-1}$. More importantly, the resulting functional composite film (SMC_x) resolutely has a stable EMI shielding and thermal insulation properties in simulated high-temperature and cold extreme environments. In conclusion, the design of this study not only effectively avoids the influence of MXene@c-MWCNT on the overall thermal insulation performance of the composite film by adjusting the number of functional unit layers, but also greatly improves the overall mechanical and EMI shielding performance; therefore, the

composite functional film obtained in this work has broad application prospects in extreme fields like aerospace.

2 Materials and Methods

2.1 Materials

Poly(vinyl alcohol) (PVA 1788), lithium fluoride (LiF, $\geq 99.9\%$), hydrochloric acid (HCl, 35%) and sodium dodecyl sulfate (SDS, AR) were obtained from Shanghai Macklin Biochemical Co., Ltd. Tetraethyl orthosilicate (TEOS, 98%) was purchased from Tianjin Kemiou Chemical Reagent Co., Ltd. Oxalic acid ($\text{H}_2\text{C}_2\text{O}_4$, AR) was provided by Tianjin Damao Chemical Reagent Factory. Ti_3AlC_2 (MAX) powder ($\leq 38 \mu\text{m}$, 98%) was supplied by 11 Technology Co., Ltd. Carboxylated multi-wall carbon nanotubes (c-MWCNT, $\geq 98\%$) were provided by Shenzhen Suiheng Technology Co., Ltd. Deionized water was supplied in unlimited quantities by the laboratory.

2.2 Preparation of SNM

Figure S1(I) shows the preparation process of SiO_2 nanofiber membranes (SNM). First, TEOS, H_2O and $\text{H}_2\text{C}_2\text{O}_4$ were mixed and stirred at room temperature at a molar ratio of 1:8.063:0.0186 for 10 h to prepare SiO_2 precursor sol. Second, SiO_2 sol and 10 wt% PVA solution were mixed at a mass ratio of 1:1 and stirred for 10 h to obtain the spinnable precursor solution [34]. Then, the SiO_2 /PVA nanofiber membranes (SPNM) were fabricated by an electrospinning device and the corresponding setting parameters were as follows: applied voltage of 14 kV, syringe boost speed of 1.1 mL h^{-1} , drum rotation speed of 140 rpm, receiving distance of 20 cm, and the relative humidity and temperature were 40%–50% and 23–25 °C, respectively [35]. Finally, SPNM were pretreated in a vacuum oven at 60 °C and then placed in a tube furnace (BTF-1700C-CVD from Anhui BEQ Equipment Technology Co., Ltd.) with a constant heating rate of $5 \text{ }^\circ\text{C min}^{-1}$ up to 800 °C for 2 h to form SNM.

2.3 Preparation of MXene@c-MWCNT_{x,y}

MXene flakes were obtained by etching Ti_3AlC_2 MAX powder with HF. Briefly, 2 g LiF was dissolved in 100 mL HCl solution (12 M) being stirred at 35 °C for 10 min. Then,

Ti_3AlC_2 powders were gradually added to the above mixture, and the reaction was held at 35 °C for 24 h. After reaction, the solid was separated with supernatant via centrifugation for 10 min at 3500 rpm. Subsequently, it was washed by deionized water and centrifuged until the pH=6 [30]. The resulting $\text{Ti}_3\text{C}_2\text{T}_x$ MXene was then dispersed in deionized water to obtain 1 mg mL^{-1} MXene dispersion.

In order to improve the solution dispersibility of c-MWCNT, c-MWCNT and a little SDS were added to deionized water and sonicated for 30 min to prepare 1 mg mL^{-1} c-MWCNT dispersion [36]. As shown in Fig. S1(II), the above two dispersions were mixed in mass ratios of 0:10, 4:6, 5:5, 6:4, and 10:0, respectively, followed by ultrasound for 30 min to prepare mixed dispersion. In the end, 50 mL mixed dispersion was filtered to prepare MXene@c-MWCNT_{x,y} with a diameter of 4 cm and a mass of 50 mg by vacuum filtration method.

2.4 Preparation of SMC_x

Figure S1(III) presents the preparation process of SMC_x. Wisely, 5 wt% PVA solution was evenly spread on the MXene@c-MWCNT_{x,y}, followed by that SNM was laid flat on it and tightly bonded the two layers under a certain pressure. After that, the obtained composite film was placed in the oven at 60 °C for 2 h to obtain SMC₁. Finally, taking SMC₁ as a unit structure, SMC₂ and SMC₃ with two and three SMC₁ were obtained by the same bonding method.

2.5 Characterization

The morphology and microstructure were observed by SEM (FESEM thermoscientific Apreo C, America). Attenuated total reflection Fourier transform infrared (ATR-FTIR) spectra in the frequency region of 4000–400 cm^{-1} at a 4 cm^{-1} resolution were recorded using an FTIR spectrometer (Nicolet 6700, America) with 32 scans. The thermogravimetric analysis (TGA) of the precursor nanofiber membrane was conducted by using a thermal gravimetric analyzer (TG209F3, Germany) in an air atmosphere, and the heating rate was $10 \text{ }^\circ\text{C min}^{-1}$. Tensile properties were measured using a universal testing machine (AG-X plus, Shimadzu Instruments) at a loading rate of 1 mm min^{-1} . The sheet resistance (R_s) was examined using an RTS-8 four-point probe, and the corresponding electrical conductivity (σ) was calculated using the equation: $\sigma = 1/$

($d \cdot R_s$) (d is the film thickness) [37]. The thermal conductivity was measured by a thermal constant analyzer (TPS2500S, Hot Disk AB, Sweden). The EMI shielding performance of the MXene@c-MWCNT_{x,y} and SMC_x were measured using an Agilent PNAN5244A vector network analyzer at room temperature in frequency ranges of 8.2–12.4 GHz (X-band), and the test samples were circular films with a diameter of 4 cm.

2.6 EMI Shielding Testing

In this test, the center of the inside sides of the test fixture is a rectangular cavity with a length of 2 cm and a width of 1 cm. The samples were made into a circle with a diameter of 4 cm to ensure that the sample can completely cover the cavity and successfully complete the experiment. When the experiment was carried out, the fixture was forcefully clamped to avoid serious EM wave exposure, so as to obtain reliable experimental data. The power coefficients of reflection (R), absorption (A) and transmission (T), as well as the total EMI SE (SET), absorption SE (SE_A), and reflection SE (SE_R) were calculated as follows [38]:

$$R = |S_{11}|^2, T = |S_{21}|^2 \quad (1)$$

$$1 = A + R + T \quad (2)$$

$$SE_T = SE_A + SE_R + SE_M \quad (3)$$

$$SE_R = -10 \log |1 - R|, SE_A = -10 \log |T/(1 - R)| \quad (4)$$

where S_{11} represents forward reflection coefficient, S_{12} represents reverse transmission coefficient, and SE_M represents the multiple reflection SE between the two surfaces of the film [39]. When $SE_T \geq 15$ dB, the SE_M can be ignored [40].

2.7 Thermal Insulation Testing

In addition to directly reflecting the thermal conductivity of the sample with the thermal constant analyzer, the thermal insulation performance of the sample was visually tested with the infrared thermal imager (E60, FLIR, America) under simulated high-temperature and cold environments. Here, infrared thermal imager is used to record real-time surface temperature changes of different samples over time. In order to ensure the reliability of the data, the initial

temperature of the samples under similar experiment (high-temperature or cold environment) needs to be consistent.

For high-temperature environment testing, Xenon lamp devices (CEL-PE300L-3A, China Education Au-light Co., Ltd, China) that release simulated sunlight can provide continuous high-temperature environment. During the experiment, the circular sample with a diameter of 4 cm was placed 15 cm perpendicular to the 300 W Xenon lamp source (Fig. S2a).

For low-temperature environment testing, a cylindrical glass container (with an inner diameter of 15 cm and a depth of 9 cm) filled with ice cubes is freshly removed from the refrigerator and covered with a layer of plastic wrap to keep the sample from getting soggy (Fig. S2b).

3 Results and Discussion

3.1 Characterization

As shown in Fig. 1a, b, compared to the digital photographs of SPNM, the SNM obtained after calcination still maintain great flexibility and its surface becomes smooth and dense. Figure 1c, d shows the SEM test results of SPNM and SNM at the same magnification, respectively. It can be seen that the fiber distribution of both is relatively uniform and the fiber diameter of SNM has been significantly decreased. By further magnifying the scanning magnification, from Fig. 1e and f, it can be clearly seen that the fiber diameter was also uniform. Fifty fibers were selected from SPNM and SNM respectively for diameter statistical analysis, and it was found that the diameter distribution of both fibers followed a normal distribution (Fig. 1g). Specifically, the fiber diameter of SPNM is generally distributed in the range of 490–550 nm, and the fiber diameter of SNM is generally distributed in the range of 350–360 nm. After statistical calculation (Table S1), the average fiber diameter of SNM decreased from 527.06 nm in SPNM to 356.03 nm.

Figure 1h presents that the TGA curves of PVA, SPNM and SNM from 30 to 900 °C in the air atmosphere. The TGA curve of PVA shows that it can be completely decomposed before 600 °C, which is consistent with the conclusion of other studies [41, 42]. It can be seen from the TGA curve of SPNM that the weight loss of SPNM is mainly concentrated in two stages: the range of 100–400 °C with a

mass loss of 27% and the range of 400–750 °C with a mass loss of 20%. The former is mainly attributed to the removal of water molecules and part of PVA, while the latter is mainly due to the removal of residual organic matter. In addition, the TGA curve of the SNM showed that its mass has hardly changed throughout the entire testing temperature range. Combined with the TGA of PVA and SPNM, it can be preliminarily concluded that the SNM obtained after heat treatment at 800 °C have a high-temperature resistance and no organic components.

So as to further analyze the components of SNM and SPNM, they were characterized by ATR-FTIR (Fig. 1i). In FTIR spectra of SPNM, the broad peaks at around 3400 and 2900 cm^{-1} were assigned to the –OH bonds and the

CH_n groups, respectively [43–45]. However, the FTIR spectra of SNM do not have the above two characteristic peaks, indicating that organic matter (such as PVA, residual TEOS and $\text{H}_2\text{C}_2\text{O}_4$) in SPNM is completely removed after being calcined at 800 °C. Moreover, the spectra only show obvious peaks near 1095 and 800 cm^{-1} , which correspond to the tensile vibration of Si–O–Si bonds [46]. The above results comprehensively indicate that SNM are mainly composed of ceramic SiO_2 phase. Combined with TGA results, it has been proven that after heat treatment at 800 °C, organic components in SPNM are completely removed, and the resulting SNM are only composed of inorganic components of SiO_2 . This conclusion also

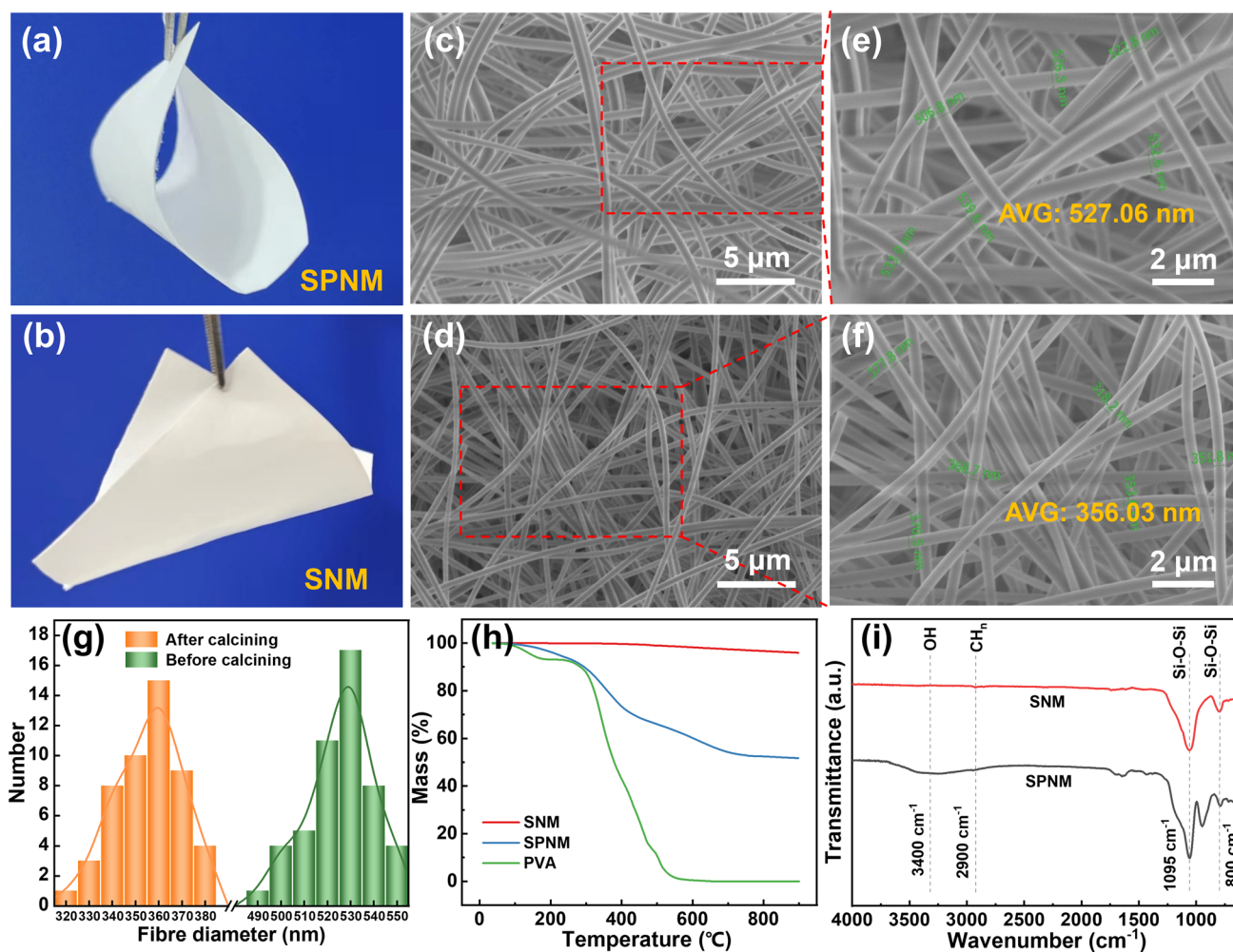


Fig. 1 a, b Digital photographs, c–f SEM images and g fiber diameter size distribution of SPNM and SNM. h TG curves of SPNM, SNM and PVA. i ATR-FTIR spectra of SPNM and SNM

effectively explains the obvious decrease in fiber diameter from SPNM to SNM.

$\text{Ti}_3\text{C}_2\text{T}_x$ MXene nanosheets with a high specific surface area are usually prepared by acid etching and ultrasonic exfoliation [47–49]. In this experiment, after the middle aluminum layer was etched off by HF, the compact massive carbon-aluminum-titanium (Ti_3AlC_2 MAX) particles (Fig. 2a) evolved into multilayered $\text{Ti}_3\text{C}_2\text{T}_x$ MXene with an accordion structure (Fig. 2b). Further ultrasonic stripping resulted in ultra-thin monolayer $\text{Ti}_3\text{C}_2\text{T}_x$ MXene (Fig. 2c) [50]. Figure 2d shows the SEM microscopic morphology of c-MWCNT, which are uniformly distributed and correspond to a product description with an inner diameter of 3–5 nm, an outer diameter of 8–15 nm, and a length of 5–15 μm . Figure 2e presents the standing experiments of MXene@MWCNT_{6:4} and MXene@c-MWCNT_{6:4} dispersions, respectively. It can be clearly seen that after being placed for 10 days, the former shows a distinct deposition separation phenomenon, while the latter still remains a uniform dispersion. After 30-day placement, more than half of the solid deposits appeared in the former, while the latter remained almost unchanged. In comparison, it can be preliminarily concluded that the active functional groups (-OH, -F, C=O, etc.) of MXene and c-MWCNT are well combined, thereby improving the overall dispersibility and antioxidant properties.

The major valence bonds of MXene, c-MWCNT and MXene@c-MWCNT_{x:y} were further analyzed by ATR-FTIR. As shown in Fig. 2f, the FTIR spectrum of MXene shows typical representative vibrational peaks, which are, respectively, attributed to the -OH bonding near 3400 and 1390 cm^{-1} , C=O bonding near 1630 cm^{-1} , C-F bonding near 1116 cm^{-1} , and Ti-O terminal group near 535 cm^{-1} [30, 51]. In addition to the aforementioned -OH and C=O characteristic peaks, the FTIR spectrum of c-MWCNT also contains C-O bonding near 1026 cm^{-1} and CH_n groups near 2900 cm^{-1} [52]. The FTIR spectrum of MXene@c-MWCNT_{6:4} contains all the characteristic peaks of MXene and c-MWCNT, indicating the formed effective valence bond binding between them. It is worth noting that the FTIR spectrum of MXene@c-MWCNT_{6:4} is similar to that of c-MWCNT (except for the Ti-O characteristic peak). This is because when MXene and c-MWCNT are mixed together, the latter wraps the former (Fig. 3j), resulting in most of the infrared beams to preferentially contact and reflect with c-MWCNT during testing.

In order to analyze the microstructures of MXene@c-MWCNT_{x:y} more thoroughly, SEM characterizations were carried out from both the surface and the cross section. As can be seen from the surface SEM images (Fig. 3a, b, c, d), with the increase in the relative content of MXene, the number of transparent MXene sheets distributed on the surface of MXene@c-MWCNT_{x:y} is gradually increased. Especially when the mass ratio of MXene:c-MWCNT reaches 6:4, the MXene sheets are in contact with each other (Fig. 3e), which helps to improve the overall electrical conductivity of MXene@c-MWCNT_{6:4}.

For the SEM images of the cross sections, similarly, the number of MXene sheets embedded in c-MWCNT gradually increases with the increase in their content (Fig. 3g, h, j). From Fig. 3j, it can be seen that MXene sheets distributed at MXene@c-MWCNT_{6:4} are dense and uniform. In addition, region A indicates that MXene sheets are enveloped by a large amount of c-MWCNT, and region B reveals that the surrounding linked c-MWCNT will be taken away when MXene is pulled out. The above two phenomena imply a strong binding force between MXene and c-MWCNT, which is provided by the hydrogen bond formed between their active functional groups (Fig. 3k) [53]. Based on the above analysis, one-dimensional c-MWCNT and uniformly embedded two-dimensional MXene form a “hand in hand” three-dimensional wire junction structure, which provides a theoretical basis for MXene@c-MWCNT_{6:4} with good electrical conductivity and mechanical properties. From Fig. 3f, l, it can be seen that a pure MXene film is formed by stacking rigid and fluffy MXene sheets.

3.2 Mechanical Tensile Performance

Both good mechanical tensile strength and flexibility are important indicators for the practical application of fiber-based composites [54–56]. As demonstrated in Fig. 4a, the tensile strength and modulus of SNM obtained by calcination are greater than that of SPNM. Figure 4b reveals that the tensile strength of MXene@c-MWCNT_{x:y} is significantly higher than that of pure MXene and c-MWCNT films, and the tensile strength of hybrid films increases with the increase in MXene content. When the weight ratio of MXene to c-MWCNT is 6:4, MXene@c-MWCNT_{6:4} reaches the maximum tensile strength of 4.28 MPa, which is mainly attributed to the strong interfacial adhesion between MXene nanosheets and c-MWCNT

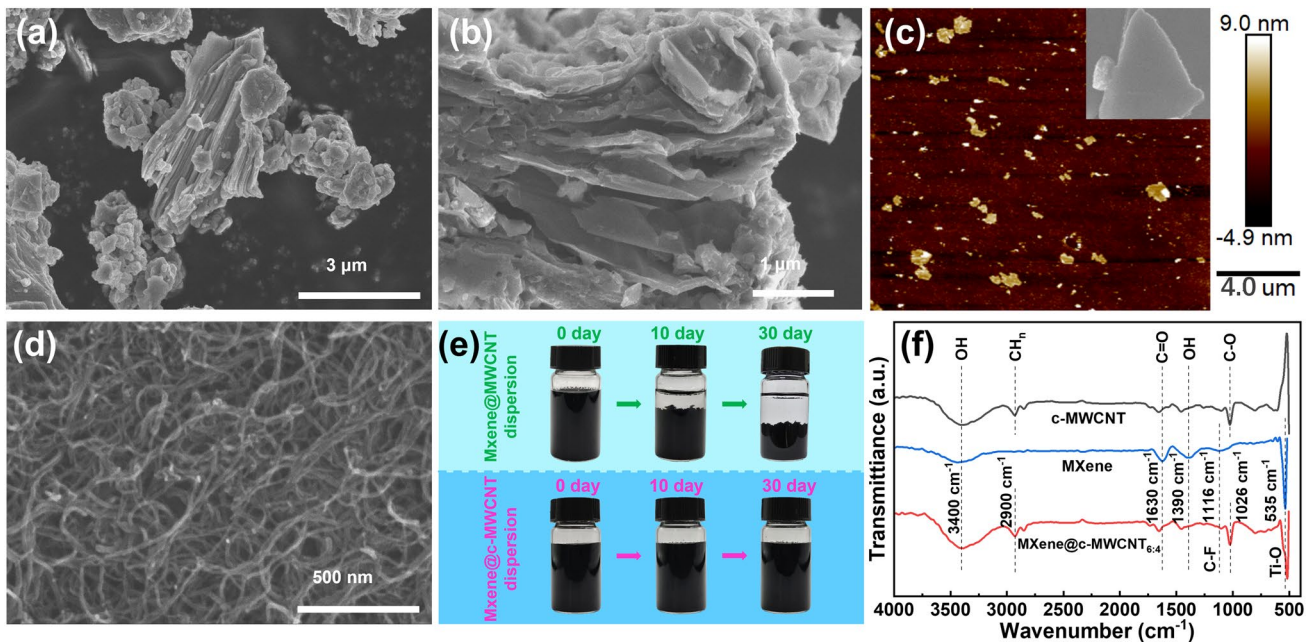


Fig. 2 **a** SEM image of Ti_3AlC_2 . **b** SEM image of multi-layer MXene without ultrasonication. **c** AFM image and SEM image (inset) of MXene monolayer. **d** SEM image of c-MWCNT. **e** Digital photograph of MXene@c-MWCNT_{6:4} and MXene@c-MWCNT_{6:4} dispersions for different static times. **f** ATR-FTIR spectra of MXene, c-MWCNT and MXene@c-MWCNT_{6:4}

through hydrogen bonding and π - π interaction [57]. However, the maximum strain of the hybrid film decreases with the increase in MXene content, which is mainly due to the weak van der Waals forces between the rigid MXene nanosheets. Through the complementary effect of c-MWCNT, it can be seen from Fig. 4b (inset) that MXene@c-MWCNT_{6:4} still has a good flexibility.

From Fig. 4c, it can be clearly seen that the tensile strength of SMC_x composite film composed of SNM/MXene@c-MWCNT_{6:4} (unit layer) has been greatly improved, especially for SMC₃ prepared by bonding three unit layers with 5 wt% PVA, which has a mechanical tensile strength of 10.01 MPa. Figure 4d, e, f shows the tensile cross sections of SMC₁, SMC₂, and SMC₃, it can be seen that SNM and MXene@c-MWCNT_{6:4} are tightly coupled, as well as between different unit layers. As shown in the insertion, the SMC₃ containing three unit structures still maintains good bendability. It is worth mentioning that the SMC_x obtained in this work realizes the micrometer level in the thickness direction (Table S2), which can greatly save space and enhance the value of practical application.

3.3 Electromagnetic Interference Shielding Performance

Electrical conductivity is one of the main factors affecting the performance of EMI shielding [58, 59]. MXene@c-MWCNT_{x:y} serve as the main contributor of EMI shielding in this work, as shown in Fig. 5a, with the increase in MXene content, the conductivity of MXene@c-MWCNT_{x:y} is significantly enhanced (MXene@c-MWCNT_{6:4} reaches 7378 S m^{-1}), while the sheet resistance and thickness of hybrid film are obviously reduced (Fig. S3 and Table S3). Here, although the pure MXene film has the highest electrical conductivity ($11,869 \text{ S m}^{-1}$), its poor mechanical stretchability limits its further application.

In Fig. 5b, the SE reflection (SE_R) curve of pure c-MWCNT film in the X-band is relatively stable, while the SE_R curves of the pure MXene film and hybrid films present wavy shape, and the EMI SE_R interval values of all films are approximately concentrated between 13–15 dB. Combining the formula $SE_R \text{ (dB)} = 20 \log(Z_0/4Z_1)$, where Z_0 and Z_1 are the impedance of free space and shielding material, respectively [60], it can be concluded that under the premise of constant spatial impedance, the two different SE_R curve

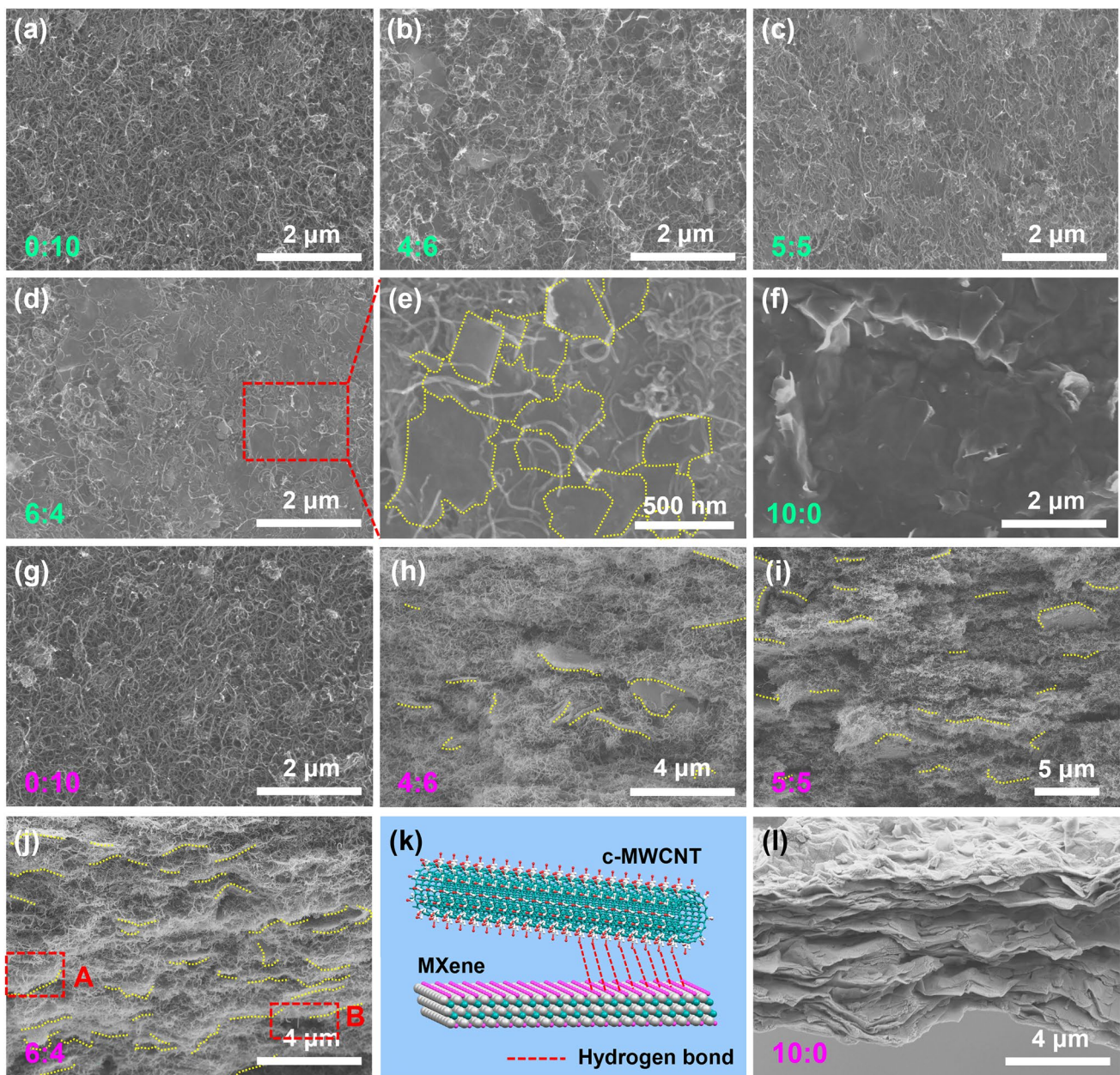


Fig. 3 SEM images of **a-f** the surface and **g-j, l** the cross section of $\text{MXene@c-MWCNT}_{x,y}$ with different weight ratio of MXene and c-MWCNT. **k** Diagram of hydrogen bond between MXene and c-MWCNT

trends are attributed to the uniform diameter distribution of one-dimensional c-MWCNT and the non-uniform diameter of two-dimensional MXene, respectively.

As shown in Fig. 5c, the SE absorption (SE_A) value of the hybrid film in the X-band is enhanced with the increase in MXene content and reaches the maximum value when the ratio of MXene to c-MWCNT is 6:4. The EMI SE_A is mainly determined by the shielding thickness (d) and skin depth (δ)

[61], and their general relationship is SE_A (dB) = $20(d/\delta) \log e = 8.686(d/\delta)$, where δ is skin depth and defined as the electromagnetic energy decreases to e^{-1} of the incident wave, it is described as $\delta = (\pi f \mu \sigma)^{-1/2}$ if $\sigma \gg 2\pi f \epsilon_0$, in which σ is the electrical conductivity, ϵ_0 is the vacuum permittivity, and permeability $\mu = \mu_0 \mu_r$ ($\mu_0 = 4\pi \times 10^{-7} \text{ H m}^{-1}$, $\mu_r = 1$), so shielding thickness (d) and the electrical conductivity (σ) are the critical factors for SE_A [62]. According to the

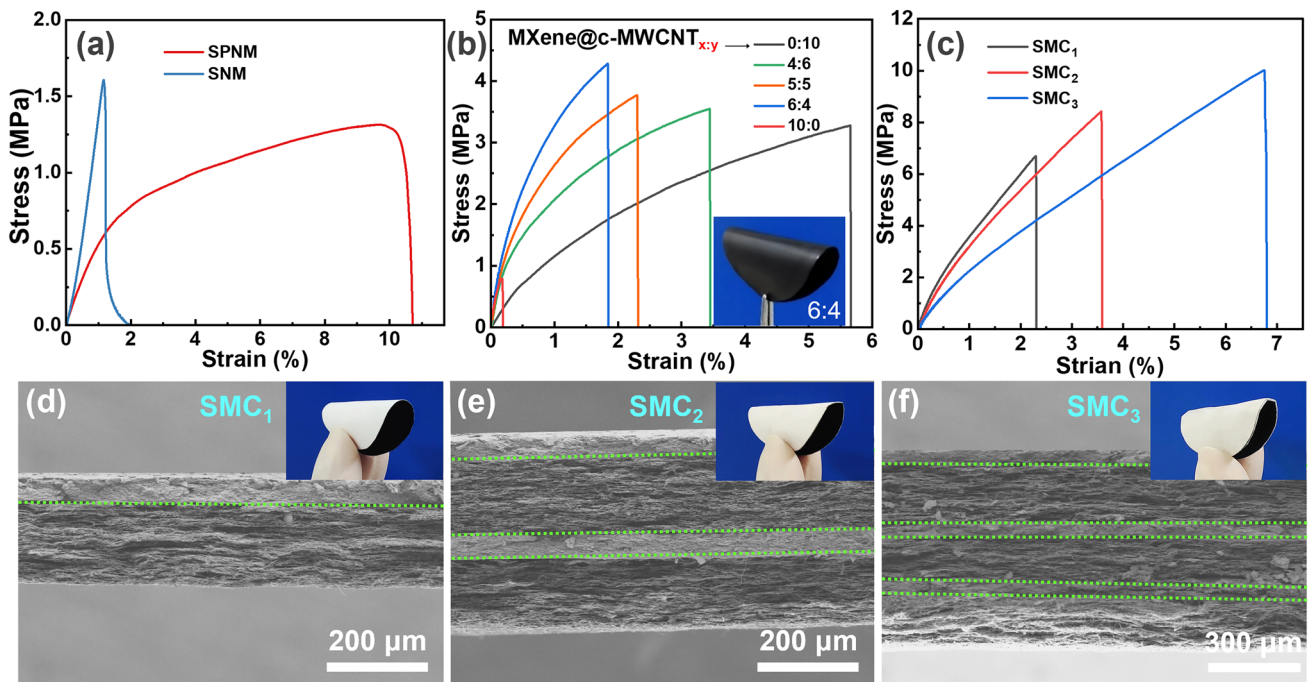


Fig. 4 Typical stress–strain curves of **a** SPNM and SNM, **b** MXene@c-MWCNT_{x,y}, and **c** SMC_x. **d–f** SEM cross-sectional images of SMC_x and corresponding digital photographs

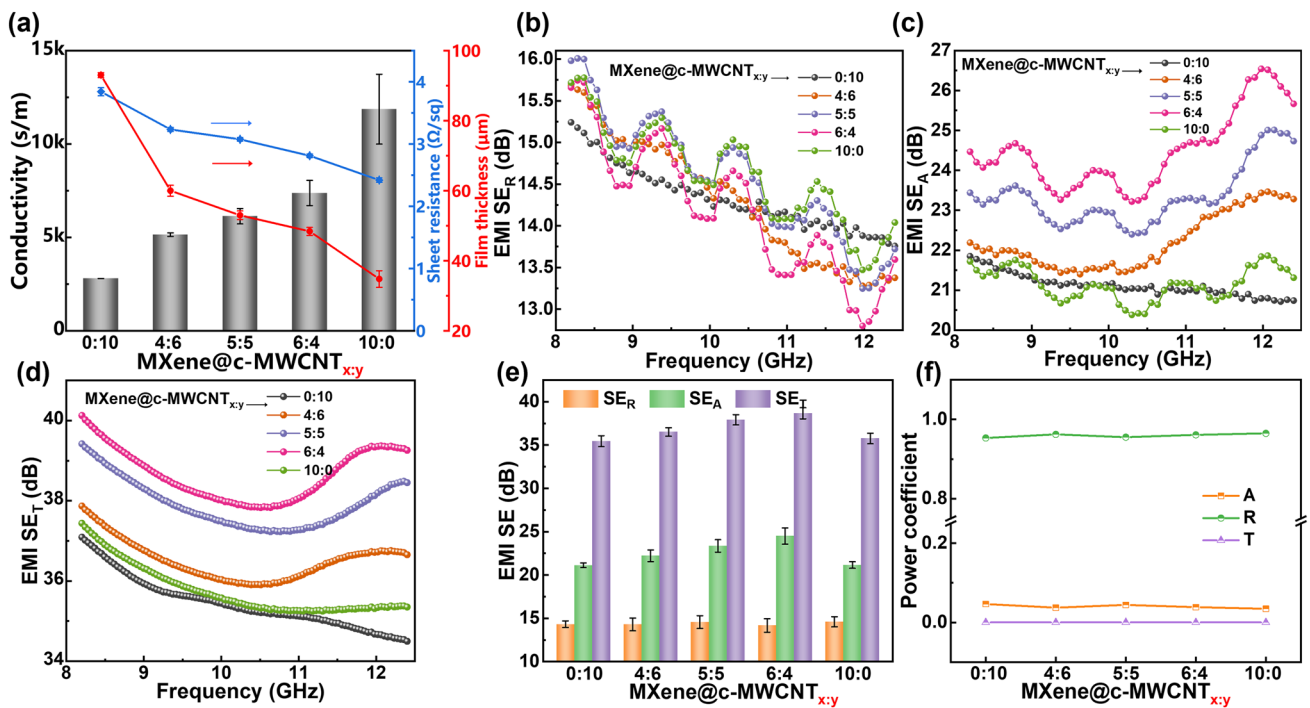


Fig. 5 **a** Conductivity, sheet resistance and film thickness, **b–d** EMI SE_T , SE_R , SE_A performance in the X-band, **e** average EMI SE_T , SE_A , SE_R values and **f** power coefficients of MXene@c-MWCNT_{x,y}

above analysis, it can be concluded that in the process of gradual change of MXene/c-MWCNT mass ratio from 0:10 to 6:4, the progress of SE_A mainly benefits from the increase in electrical conductivity (σ) (Fig. 5a), but when the ratio transitions from 6:4 to 10:0, the decrease in SE_A is mainly attributable to a sharp reduction in the thickness (d) of the shielding film (Table S3). In addition, as shown in Fig. 5d, the change trend of EMI shielding effectiveness total (SE_T) is consistent with that of SE_A .

The average values of SE_T , SE_A , and SE_R in the X-band of the sample can effectively disclose its electromagnetic shielding mechanism. It can be clearly seen from Fig. 5e that the SE_T values of MXene@c-MWCNT_{x:y} are all greater than 30 dB, which indicates that they can meet the actual requirements in various fields [63]. Combined with the double advantages of electrical conductivity and thickness, the SE_T average value of MXene@c-MWCNT_{6:4} is as high as 38.66 dB. According to the shielding efficiency formula η (%) = $100 - 100(1/10^{SE/10})$ [62], MXene@c-MWCNT_{6:4} can shield 99.98% of incident electromagnetic wave. In addition, the SE_R values of all films are stable in the range of 15 dB, indicating that more than 90% of the incident electromagnetic wave is shielded by reflection [64].

Although the SE_A values of the shielding films in Fig. 5e are higher than the SE_R values, most electromagnetic waves are reflected before entering the shielding layer, so the power coefficient of EMI shielding needs be further analyzed [65]. The power coefficient includes absorption coefficient (A), reflection coefficient (R) and transmission coefficient (T), which are used to evaluate the ability of EMI shielding materials to absorb, reflect and transmit electromagnetic waves, respectively [66]. Figure 5f shows that the T values of the shielding films are close to 0, indicating that MXene@c-MWCNT_{x:y} can shield almost all incident electromagnetic waves. At the same time, the much higher R values than A values indicate that MXene@c-MWCNT_{x:y} mainly follow a reflectance-based electromagnetic shielding mechanism.

The number of structural unit layers contained in SMC_x is an important factor affecting the electromagnetic shielding performance. As shown in Fig. 6a, b, c, the SE_R and SE_A of composite film SMC_x in X-band both rise with the increase in the number of structural unit layers, and SE_T of SMC₃ is greatly improved compared with SMC₁ and SMC₂. SMC₁ can only reflect and absorb electromagnetic waves on one side, while the EMI shielding mechanism of SMC₂ and SMC₃ also includes multiple reflections and multiple

absorption, so the SE_T increases with the increase in the number of layers of structural units. Therefore, the average SE_T of SMC₁, SMC₂, and SMC₃ in Fig. 6d is 37.80, 46.00, and 55.40 dB, respectively. After calculation, SMC₃ can shield 99.99% of incident electromagnetic wave. Similar to MXene@c-MWCNT_{x:y}, it can be seen from Fig. 6e that the main shielding mechanism of SMC_x is also reflection. In order to explore the durability of the electromagnetic interference shielding characteristics of SMC₃, a series of extreme environment tests have been carried out. As shown in Fig. 6f, after being bent 50 times, baked at high-temperature (about 500 °C) for 10 min, and frozen in liquid nitrogen for 2 h, the average SE_T value of SMC₃ is still as high as 54.37 dB, indicating that the SMC_x has excellent EMI shielding durability.

3.4 Thermal Insulation Performance

For composite films (SMC_x), MXene@c-MWCNT_{6:4} serves as a functional layer for EMI shielding (Fig. 5), while SNM layer gives an excellent thermal insulation performance. In Fig. 7a, the thermal conductivity of SNM (0.034 W m⁻¹ k⁻¹) is lower than that of SPNM (0.037 W m⁻¹ k⁻¹), which is mainly due to the elimination of PVA and other organics in SPNM after high-temperature calcination, realizing SNM composed of pure SiO₂ ceramic fiber. Although MXene (472 W m⁻¹ k⁻¹) and CNT (700 W m⁻¹ k⁻¹) have considerable theoretical thermal conductivity [32, 67], the SMC_x obtained by combining the SNM layer still maintain the ideal thermal insulation effect, and the thermal conductivities of SMC₁, SMC₂ and SMC₃ are 0.066, 0.064, and 0.062 W m⁻¹ k⁻¹, respectively. This not only shows that SMC_x can effectively overcome the influence of the high thermal conductivity of the shielding film (MXene@c-MWCNT_{6:4}) and maintain the excellent thermal insulation property of SNM, but also reveals that the thermal conductivity of SMC_x decreases gradually with the increase in the number of structural unit layers.

In order to more intuitively reflect the thermal insulation performance of SMC_x, real-time monitoring of their thermal management performance in simulated high and low temperature environments is carried out using an infrared thermal camera [68]. For the high-temperature environment created by Xenon lamp, as shown in Fig. 7b, the surface temperature of MXene@c-MWCNT_{6:4} reaches above

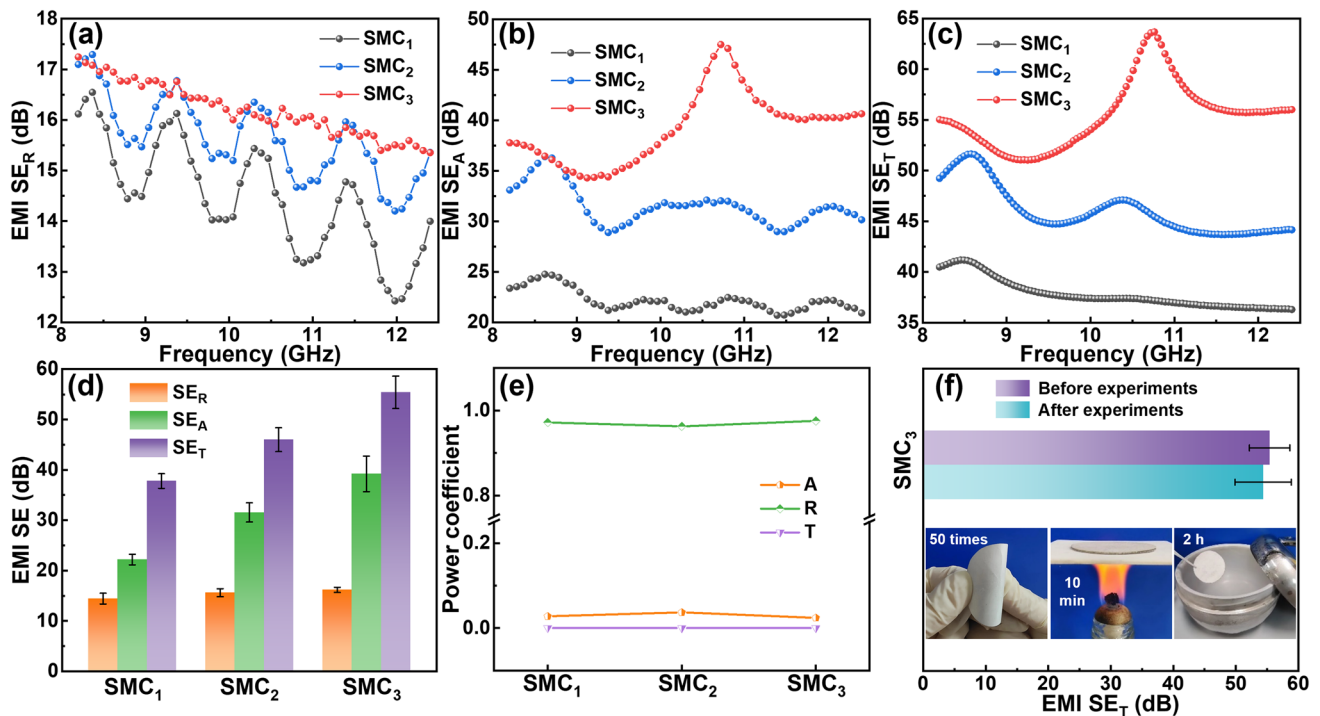


Fig. 6 a-c EMI SE_R, SE_A, and SE_T performance, d average EMI SE_T, SE_A, SE_R values and e power coefficients of SMC_x. f EMI shielding performance of SMC₃ after a series of extreme environment tests

120 °C instantaneously and is stabilized at about 135 °C after 40 s. In contrast, SNM showed excellent thermal insulation performance, with a surface temperature maintained at around 65 °C after 60 s. In addition, the thermal insulation effect of SMC_x obtained by bonding the shielding layer MXene@c-MWCNT_{6,4} and SNM with PVA has been further improved. From the infrared thermal imaging in Fig. 7c, it can be clearly seen that the final temperatures of SMC_x are all around 60 °C. It is worth mentioning that the thermal insulation performance of SMC_x did not gradually increase with the increase in structural units, mainly due to the certain photothermal conversion ability of MXene and CNT [69]. The natural cooling experiment after 60 s further verified the low thermal diffusion coefficient of SMC_x.

For the low temperature environment created by ice, the temperature is maintained at about -2.5 °C. As shown in Fig. 7d, the cooling rates of SNM, SMC₁, SMC₂, and SMC₃ decreased successively for different fiber films placed in the cold environment at the same time. Importantly, the temperature protection capacity of SMC_x at low temperature increased with the increase in the number of unit layers, corresponding to SMC₁: 15.46 °C, SMC₂: 17.23 °C and

SMC₃: 20.18 °C, respectively (Fig. 7e). Interestingly, the minimum temperature of SMC₁ is similar to that of SNM, which should be because SMC₁ only contains one layer of SNM, making its thermal insulation performance very close to that of SNM. In summary, SMC_x shows excellent thermal insulation and heat preservation for extreme thermal and cold environments, respectively.

3.5 Dual-Effect Mechanism of EMI Shielding and Heat Insulation

Combined with the above analysis results, SMC_x shows dual effects of EMI shielding and thermal insulation. For EMI shielding, MXene@c-MWCNT_{6,4} layer play a major role, as shown in Fig. 8I, when electromagnetic waves reach the surface of the shielding film, more than 90% of the electromagnetic waves are immediately reflected due to the impedance mismatching of the surface free electrons [70]. Next, the interaction between the incident electromagnetic waves and the high density of electrons and holes in the conductive layer causes conductive loss, weakening

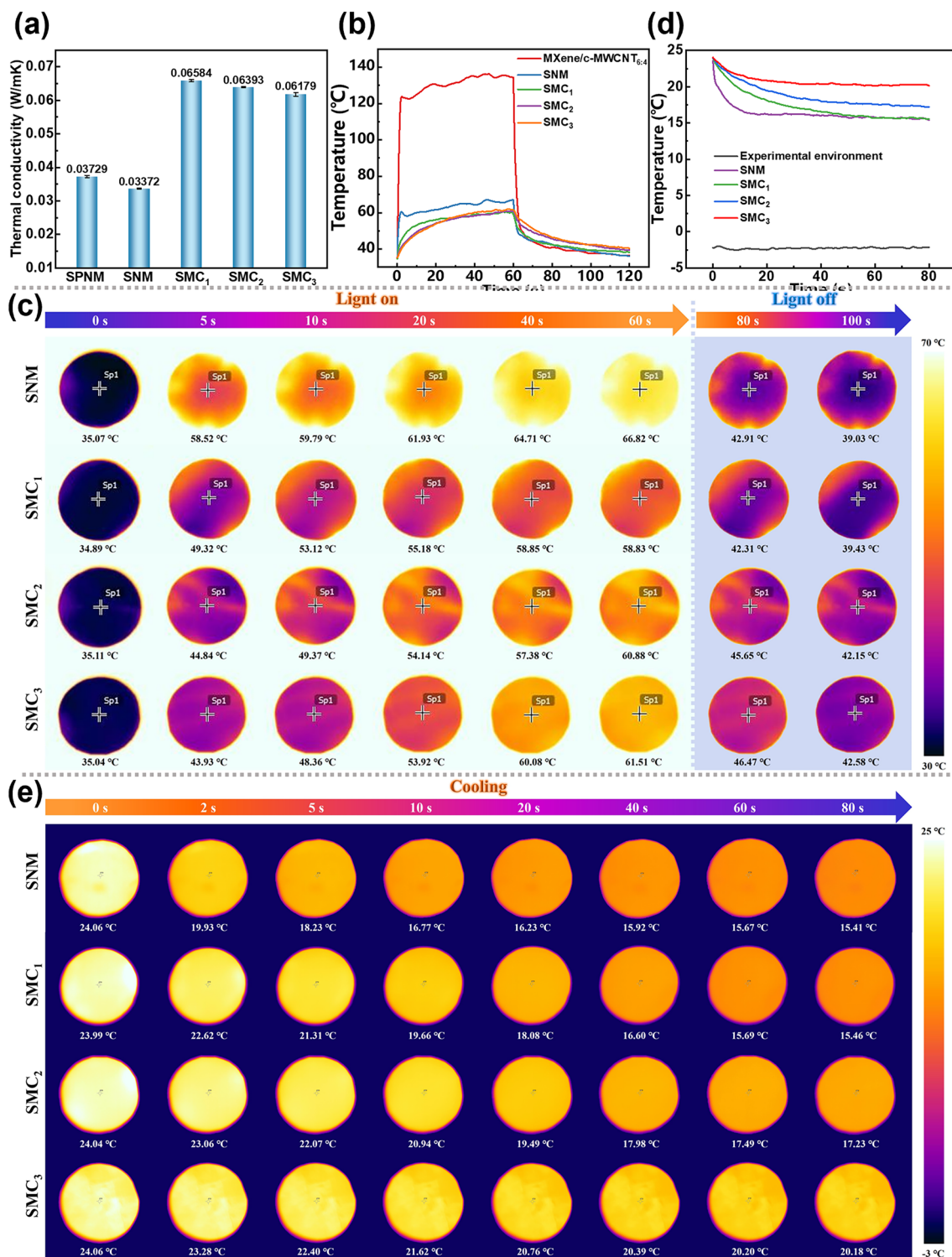


Fig. 7 **a** Thermal conductivity of SPNM, SNM and SMC_x. **b** Temperature–time curves and **c** corresponding infrared images of MXene@c-MWCNT_{6,4}, SNM and SMC_x in high-temperature environment. **d** Temperature–time curves and **e** corresponding infrared images of SNM and SMC_x in extreme cold environment

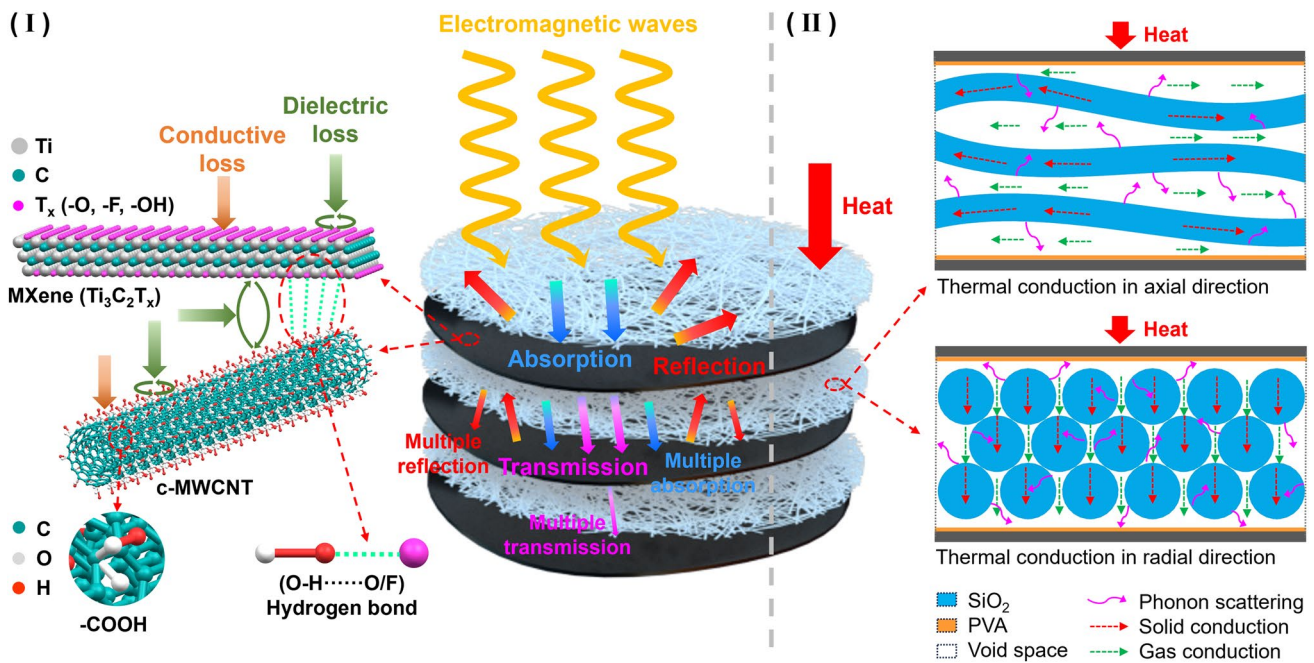


Fig. 8 I EMI shielding and II thermal insulation mechanism diagram of SMC_x

the power of the incident electromagnetic waves. In addition, the abundant active groups and heterogeneous interfaces provided by MXene and c-MWCNT induce both dipole and interfacial polarizations, further absorbing the energy of incident electromagnetic waves [71]. Therefore, after a series of reflections and absorption, only a very small amount of transmitted electromagnetic waves enter the next shielding layer. As a result, after multiple reflections and absorptions, almost no electromagnetic waves can penetrate the SMC_3 .

For thermal insulation, SNM layer play a major role, as shown in Fig. 8II, due to the small aperture between SiO_2 fibers, the convective heat transfer can be almost negligible, so the total thermal conductivity (λ_t) for SMC_x can be represented as the sum of contributions from three parts ($\lambda_t = \lambda_s + \lambda_g + \lambda_r$) [72], i.e., the solid thermal conductivity (λ_s), the gas thermal conductivity (λ_g) and the radiation thermal conductivity (λ_r). The thermal insulation mechanisms could be explained from the following four aspects: First, the extremely high length-to-diameter ratio and irregular winding of SiO_2 fibers prolong the path of heat conduction in solids; moreover, the intrinsic thermal conductivity of SiO_2 is low, leading a small λ_s . Second, the high porosity of SNM makes the air heat transfer

discontinuous in the whole space of SMC_x , contributing a low λ_g ; third, the porous structure makes the infrared radiation multiple reflect and absorb, resulting in lowering of λ_r ; finally and most importantly, the phase interface between different solids as well as between solids and voids enhances phonon scattering [73].

4 Conclusion

In this work, SNM with low thermal conductivity ($0.034 \text{ W m}^{-1} \text{ K}^{-1}$) was prepared by electrospinning followed with calcination and played a decisive role in the thermal insulation performance of SMC_x . The hybrid film composed of MXene and c-MWCNT was successfully prepared through vacuum assisted filtration, and the obtained $MXene@c-MWCNT_{x,y}$ showed good EMI shielding performance. When the weight ratio of MXene to c-MWCNT was 6:4, $MXene@c-MWCNT_{6,4}$ exhibited excellent comprehensive performance in terms of tensile strength (4.28 MPa) and EMI shielding (SE_T 38.66 dB). Finally, SMC_x with good EMI shielding and thermal insulation performance was successfully prepared by using 5 wt% PVA as an adhesive. Specifically, the thermal conductivities of SMC_1 , SMC_2 and SMC_3 are 0.066, 0.064, and $0.062 \text{ W m}^{-1} \text{ K}^{-1}$,

and their EMI SE_T are 37.80, 46.00, and 55.40 dB respectively. In addition, the overall performance of SMC_x was improved with the increase in the number of structural unit layers. Importantly, SMC_x presents good durability in extreme hot and cold environments. The design ideas of this work have an important reference value for the development of special equipment such as manned space suits.

Acknowledgements We acknowledge for the China Scholarship Council (2021). The authors extend their appreciation to the Deanship of Scientific Research at Northern Border University, Arar, KSA for funding this research work through the project number “NBU-FPEJ-2024-249-03”.

Declarations

Conflict of interests The authors declare no interest conflict. They have no known competing financial interests or personal relationships that could have appeared to influence the work reported in this paper. Zhanhu Guo is an editorial board member for Nano-Micro Letters and was not involved in the editorial review or the decision to publish this article. All authors declare that there are no competing interests.

Open Access This article is licensed under a Creative Commons Attribution 4.0 International License, which permits use, sharing, adaptation, distribution and reproduction in any medium or format, as long as you give appropriate credit to the original author(s) and the source, provide a link to the Creative Commons licence, and indicate if changes were made. The images or other third party material in this article are included in the article’s Creative Commons licence, unless indicated otherwise in a credit line to the material. If material is not included in the article’s Creative Commons licence and your intended use is not permitted by statutory regulation or exceeds the permitted use, you will need to obtain permission directly from the copyright holder. To view a copy of this licence, visit <http://creativecommons.org/licenses/by/4.0/>.

Supplementary Information The online version contains supplementary material available at <https://doi.org/10.1007/s40820-024-01398-1>.

References

1. P. Weiss, M.P. Mohamed, T. Gobert, Y. Chouard, N. Singh et al., Advanced materials for future lunar extravehicular activity space suit. *Adv. Mater. Technol.* **5**, 2000028 (2020). <https://doi.org/10.1002/admt.202000028>
2. Z. Han, Y. Song, J. Wang, S. Li, D. Pan et al., Research progress of thermal insulation materials used in spacesuits. *ES Energy Environ.* **21**, 947 (2023). <https://doi.org/10.30919/eesee947>
3. J. Yang, H. Wang, Y. Zhang, H. Zhang, J. Gu, Layered structural PBAT composite foams for efficient electromagnetic interference shielding. *Nano-Micro Lett.* **16**, 31 (2023). <https://doi.org/10.1007/s40820-023-01246-8>
4. D. An, Y. Chen, R. He, H. Yu, Z. Sun et al., The polymer-based thermal interface materials with improved thermal conductivity, compression resilience, and electromagnetic interference shielding performance by introducing uniformly melamine foam. *Adv. Compos. Hybrid Mater.* **6**, 136 (2023). <https://doi.org/10.1007/s42114-023-00709-1>
5. M. Clausi, M. Zahid, A. Shayganpour, I.S. Bayer, Polyimide foam composites with nano-boron nitride (BN) and silicon carbide (SiC) for latent heat storage. *Adv. Compos. Hybrid Mater.* **5**, 798–812 (2022). <https://doi.org/10.1007/s42114-022-00426-1>
6. A. Riahi, M.B. Shafii, Experimental evaluation of a vapor compression cycle integrated with a phase change material storage tank for peak load shaving. *Eng. Sci.* **23**, 870 (2023). <https://doi.org/10.30919/es8d870>
7. X. Zhao, K. Ruan, H. Qiu, X. Zhong, J. Gu, Fatigue-resistant polyimide aerogels with hierarchical cellular structure for broadband frequency sound absorption and thermal insulation. *Adv. Compos. Hybrid Mater.* **6**, 171 (2023). <https://doi.org/10.1007/s42114-023-00747-9>
8. Z. Li, D. Pan, Z. Han, D.J.P. Kumar, J. Ren et al., Boron nitride whiskers and nano alumina synergistically enhancing the vertical thermal conductivity of epoxy-cellulose aerogel nanocomposites. *Adv. Compos. Hybrid Mater.* **6**, 224 (2023). <https://doi.org/10.1007/s42114-023-00804-3>
9. L. Yin, J. Xu, B. Zhang, L. Wang, W. Tao et al., A facile fabrication of highly dispersed CeO_2/SiO_2 aerogel composites with high adsorption desulfurization performance. *Chem. Eng. J.* **428**, 132581 (2022). <https://doi.org/10.1016/j.cej.2021.132581>
10. S. Karamikamkar, H.E. Naguib, C.B. Park, Advances in precursor system for silica-based aerogel production toward improved mechanical properties, customized morphology, and multifunctionality: a review. *Adv. Colloid Interface Sci.* **276**, 102101 (2020). <https://doi.org/10.1016/j.cis.2020.102101>
11. M. Liu, H. Wu, Y. Wang, J. Ren, D.A. Alshammari et al., Flexible cementite/ferroferic oxide/silicon dioxide/carbon nanofibers composite membrane with low-frequency dispersion weakly negative permittivity. *Adv. Compos. Hybrid Mater.* **6**, 217 (2023). <https://doi.org/10.1007/s42114-023-00799-x>
12. C. Liu, S. Wang, N. Wang, J. Yu, Y.-T. Liu et al., From 1D nanofibers to 3D nanofibrous aerogels: a marvellous evolution of electrospun SiO_2 nanofibers for emerging applications. *Nano-Micro Lett.* **14**, 194 (2022). <https://doi.org/10.1007/s40820-022-00937-y>
13. Y. Si, X. Mao, H. Zheng, J. Yu, B. Ding, Silica nanofibrous membranes with ultra-softness and enhanced tensile strength for thermal insulation. *RSC Adv.* **5**, 6027–6032 (2015). <https://doi.org/10.1039/C4RA12271B>
14. D.P. Yu, Q.L. Hang, Y. Ding, H.Z. Zhang, Z.G. Bai et al., Amorphous silica nanowires: intensive blue light emitters.

- Appl. Phys. Lett. **73**, 3076–3078 (1998). <https://doi.org/10.1063/1.122677>
15. L. Wang, S. Tomura, F. Ohashi, M. Maeda, M. Suzuki et al., Synthesis of single silica nanotubes in the presence of citric acid. *J. Mater. Chem.* **11**, 1465–1468 (2001). <https://doi.org/10.1039/B010189N>
 16. J. Niu, J. Sha, Z. Liu, Z. Su, J. Yu et al., Silicon nano-wires fabricated by thermal evaporation of silicon wafer. *Phys. E Low Dimension. Syst. Nanostruct.* **24**, 268–271 (2004). <https://doi.org/10.1016/j.physe.2004.04.040>
 17. Z. Zhang, Y. Zhao, Z. Li, L. Zhang, Z. Liu et al., Synthesis of carbon/SiO₂ core-sheath nanofibers with Co-Fe nanoparticles embedded in via electrospinning for high-performance microwave absorption. *Adv. Compos. Hybrid Mater.* **5**, 513–524 (2022). <https://doi.org/10.1007/s42114-021-00350-w>
 18. S. Chanthee, C. Asavatesanupap, D. Sertphon, T. Nakkhong, N. Subjalearndee et al., Electrospinning with natural rubber and Ni doping for carbon dioxide adsorption and supercapacitor applications. *Eng. Sci.* **27**, 975 (2024). <https://doi.org/10.30919/es975>
 19. H. Mhetre, Y. Kanse, Y. Chendake, Influence of Electrospinning voltage on the diameter and properties of 1-dimensional zinc oxide nanofiber. *ES Mater. Manuf.* **20**, 838 (2023). <https://doi.org/10.30919/esmm5f838>
 20. T. Sirimekanont, P. Supaphol, K. Sombatmankhong, Titanium (IV) oxide composite hollow nanofibres with silver oxide outgrowth by combined sol–gel and electrospinning techniques and their potential applications in energy and environment. *Adv. Compos. Hybrid Mater.* **6**, 115 (2023). <https://doi.org/10.1007/s42114-023-00690-9>
 21. J. Cheng, C. Li, Y. Xiong, H. Zhang, H. Raza et al., Recent advances in design strategies and multifunctionality of flexible electromagnetic interference shielding materials. *Nano-Micro Lett.* **14**, 80 (2022). <https://doi.org/10.1007/s40820-022-00823-7>
 22. A. Udayakumar, P. Dhandapani, S. Ramasamy, S. Angaiah, Layered double hydroxide (LDH)–MXene nanocomposite for electrocatalytic water splitting: current status and perspective. *ES Energy Environ.* **24**, 901 (2023). <https://doi.org/10.30919/esee901>
 23. S. Zheng, N. Wu, Y. Liu, Q. Wu, Y. Yang et al., Multifunctional flexible, crosslinked composites composed of trashed MXene sediment with high electromagnetic interference shielding performance. *Adv. Compos. Hybrid Mater.* **6**, 161 (2023). <https://doi.org/10.1007/s42114-023-00741-1>
 24. B. Li, N. Wu, Q. Wu, Y. Yang, F. Pan et al., From “100%” utilization of MAX/MXene to direct engineering of wearable, multifunctional E-textiles in extreme environments. *Adv. Funct. Mater.* **33**, 2307301 (2023). <https://doi.org/10.1002/adfm.202307301>
 25. N.M. Soudagar, V.K. Pandit, V.M. Nikale, S.G. Thube, S.S. Joshi et al., Influence of surfactant on the supercapacitive behavior of polyaniline-carbon nanotube composite thin films. *ES Gen.* **2**, 1018 (2023). <https://doi.org/10.30919/esg1018>
 26. S.S. Wagh, D.B. Salunkhe, S.P. Patole, S. Jadkar, R.S. Patil et al., Zinc oxide decorated carbon nanotubes composites for photocatalysis and antifungal application. *ES Energy Environ.* **21**, 945 (2023). <https://doi.org/10.30919/esee945>
 27. A. Huang, Y. Guo, Y. Zhu, T. Chen, Z. Yang et al., Durable washable wearable antibacterial thermoplastic polyurethane/carbon nanotube@silver nanoparticles electrospun membrane strain sensors by multi-conductive network. *Adv. Compos. Hybrid Mater.* **6**, 101 (2023). <https://doi.org/10.1007/s42114-023-00684-7>
 28. C. Pramanik, J.R. Gissinger, S. Kumar, H. Heinz, Carbon nanotube dispersion in solvents and polymer solutions: mechanisms, assembly, and preferences. *ACS Nano* **11**, 12805–12816 (2017). <https://doi.org/10.1021/acsnano.7b07684>
 29. T. Xu, Y. Wang, K. Liu, Q. Zhao, Q. Liang et al., Ultralight MXene/carbon nanotube composite aerogel for high-performance flexible supercapacitor. *Adv. Compos. Hybrid Mater.* **6**, 108 (2023). <https://doi.org/10.1007/s42114-023-00675-8>
 30. B. Zhou, Y. Li, Z. Li, J. Ma, K. Zhou et al., Fire/heat-resistant, anti-corrosion and folding Ti₂C₃T_x MXene/single-walled carbon nanotube films for extreme-environmental EMI shielding and solar-thermal conversion applications. *J. Mater. Chem. C* **9**, 10425–10434 (2021). <https://doi.org/10.1039/d1tc00289a>
 31. Q. Gao, Y. Pan, G. Zheng, C. Liu, C. Shen et al., Flexible multilayered MXene/thermoplastic polyurethane films with excellent electromagnetic interference shielding, thermal conductivity, and management performances. *Adv. Compos. Hybrid Mater.* **4**, 274–285 (2021). <https://doi.org/10.1007/s42114-021-00221-4>
 32. H. Zhan, Y.W. Chen, Q.Q. Shi, Y. Zhang, R.W. Mo et al., Highly aligned and densified carbon nanotube films with superior thermal conductivity and mechanical strength. *Carbon* **186**, 205–214 (2022). <https://doi.org/10.1016/j.carbon.2021.09.069>
 33. D. Kong, Z.M. El-Bahy, H. Algadi, T. Li, S.M. El-Bahy et al., Highly sensitive strain sensors with wide operation range from strong MXene-composited polyvinyl alcohol/sodium carboxymethylcellulose double network hydrogel. *Adv. Compos. Hybrid Mater.* **5**, 1976–1987 (2022). <https://doi.org/10.1007/s42114-022-00531-1>
 34. X. Guan, Q. Zhang, C. Dong, R. Zhang, M. Peng et al., A first-principles study of Janus monolayer MXY (M = Mo, W; X, Y = S, Se, Te)/SiO₂ van der Waals heterojunctions for integrated optical fibers. *Adv. Compos. Hybrid Mater.* **5**, 3232–3244 (2022). <https://doi.org/10.1007/s42114-022-00557-5>
 35. Y. Yu, Y. Huang, L. Li, L. Huang, S. Zhang, Silica ceramic nanofiber membrane with ultra-softness and high temperature insulation. *J. Mater. Sci.* **57**, 4080–4091 (2022). <https://doi.org/10.1007/s10853-022-06913-6>
 36. S. Zhang, B. Cheng, Z. Jia, Z. Zhao, X. Jin et al., The art of framework construction: hollow-structured materials toward high-efficiency electromagnetic wave absorption. *Adv. Compos. Hybrid Mater.* **5**, 1658–1698 (2022). <https://doi.org/10.1007/s42114-022-00514-2>
 37. D.-Q. Zhang, T.-T. Liu, J.-C. Shu, S. Liang, X.-X. Wang et al., Self-assembly construction of WS₂-rGO architecture



- with green EMI shielding. *ACS Appl. Mater. Interfaces* **11**, 26807–26816 (2019). <https://doi.org/10.1021/acsami.9b06509>
38. R.B.J. Chandra, B. Shivamurthy, S.B.B. Gowda, M.S. Kumar, Flexible linear low-density polyethylene laminated aluminum and nickel foil composite tapes for electromagnetic interference shielding. *Eng. Sci.* **21**, 777 (2023). <https://doi.org/10.30919/es8d777>
39. Z. Zeng, F. Jiang, Y. Yue, D. Han, L. Lin et al., Flexible and ultrathin waterproof cellular membranes based on high-conjunction metal-wrapped polymer nanofibers for electromagnetic interference shielding. *Adv. Mater.* **32**, e1908496 (2020). <https://doi.org/10.1002/adma.201908496>
40. T. Gao, Y. Ma, L. Ji, Y. Zheng, S. Yan et al., Nickel-coated wood-derived porous carbon (Ni/WPC) for efficient electromagnetic interference shielding. *Adv. Compos. Hybrid Mater.* **5**, 2328–2338 (2022). <https://doi.org/10.1007/s42114-022-00420-7>
41. J.-L. Shie, Y.-H. Chen, C.-Y. Chang, J.-P. Lin, D.-J. Lee et al., Thermal pyrolysis of poly(vinyl alcohol) and its major products. *Energy Fuels* **16**, 109–118 (2002). <https://doi.org/10.1021/ef010082s>
42. Z. Zhang, J. Liu, F. Wang, J. Kong, X. Wang, Fabrication of bulk macroporous zirconia by combining sol–gel with calcination processes. *Ceram. Int.* **37**(7), 2549–2553 (2011). <https://doi.org/10.1016/j.ceramint.2011.03.054>
43. Z. Wu, X. Wang, S.H.K. Annamareddy, S. Gao, Q. Xu et al., Dielectric properties and thermal conductivity of polyvinylidene fluoride synergistically enhanced with silica@multi-walled carbon nanotubes and boron nitride. *ES Mater. Manuf.* **22**, 847 (2023). <https://doi.org/10.30919/esmm5f847>
44. C. Lin, Y. Zhang, S. Zhang, X.X. Wang, J. Yang et al., Facile fabrication of a novel g-C₃N₄/CdS composites catalysts with enhanced photocatalytic performances. *ES Energy Environ.* **20**, 860 (2023). <https://doi.org/10.30919/esee8c860>
45. H. Algadi, T. Das, J. Ren, H. Li, High-performance and stable hybrid photodetector based on a monolayer molybdenum disulfide (MoS₂)/nitrogen doped graphene quantum dots (NH₂ GQDs)/all-inorganic (CsPbBr₃) perovskite nanocrystals triple junction. *Adv. Compos. Hybrid Mater.* **6**, 56 (2023). <https://doi.org/10.1007/s42114-023-00634-3>
46. Q. Hu, H. Suzuki, H. Gao, H. Araki, W. Yang et al., High-frequency FTIR absorption of SiO₂/Si nanowires. *Chem. Phys. Lett.* **378**, 299–304 (2003). <https://doi.org/10.1016/j.cplett.2003.07.015>
47. V.S. Sivasankarapillai, T.S.K. Sharma, K.-Y. Hwa, S.M. Wabaidur, S. Angaiah et al., MXene based sensing materials: current status and future perspectives. *ES Energy Environ.* **15**, 4–14 (2022). <https://doi.org/10.30919/esee8c618>
48. N. Wu, Y. Yang, C. Wang, Q. Wu, F. Pan et al., Ultrathin cellulose nanofiber assisted ambient-pressure-dried, ultralight, mechanically robust, multifunctional MXene aerogels. *Adv. Mater.* **35**, e2207969 (2023). <https://doi.org/10.1002/adma.202207969>
49. J. Wang, H. Kang, H. Ma, Y. Liu, Z. Xie et al., Super-fast fabrication of MXene film through a combination of ion induced gelation and vacuum-assisted filtration. *Eng. Sci.* **15**, 57–66 (2021). <https://doi.org/10.30919/es8d446>
50. Y. Cao, M. Weng, M.H.H. Mahmoud, A.Y. Elnaggar, L. Zhang et al., Flame-retardant and leakage-proof phase change composites based on MXene/polyimide aerogels toward solar thermal energy harvesting. *Adv. Compos. Hybrid Mater.* **5**, 1253–1267 (2022). <https://doi.org/10.1007/s42114-022-00504-4>
51. Y. Wei, W. Luo, Z. Zhuang, B. Dai, J. Ding et al., Fabrication of ternary MXene/MnO₂/polyaniline nanostructure with good electrochemical performances. *Adv. Compos. Hybrid Mater.* **4**, 1082–1091 (2021). <https://doi.org/10.1007/s42114-021-00323-z>
52. F. Jia, Z. Lu, S. Li, J. Zhang, Y. Liu et al., Asymmetric c-MWCNT/AgNWs/PANFs hybrid film constructed by tailoring conductive-blocks strategy for efficient EMI shielding. *Carbon* **217**, 118600 (2024). <https://doi.org/10.1016/j.carbon.2023.118600>
53. B. Dai, Y. Ma, F. Dong, J. Yu, M. Ma et al., Overview of MXene and conducting polymer matrix composites for electromagnetic wave absorption. *Adv. Compos. Hybrid Mater.* **5**, 704–754 (2022). <https://doi.org/10.1007/s42114-022-00510-6>
54. S. Kowshik, U.S. Rao, S. Sharma, P. Hiremath, R. Prasad K.S., et al., Mechanical properties of eggshell filled non-post-cured and post-cured GFRP composites: a comparative study. *ES Mater. Manuf.* **22**, 1043 (2023). <https://doi.org/10.30919/esmm1043>
55. W. Zou, X. Zheng, X. Hu, J. Huang, G. Wang et al., Recent Advances in Injection Molding of Carbon Fiber Reinforced Thermoplastic Polymer Composites: A Review. *ES. Gen.* **1**, 938 (2023). <https://doi.org/10.30919/esg938>
56. V. Managuli, Y.S. Bothra, S. Sujith Kumar, P. Gaur, P.L. Chandracharya et al., Overview of mechanical characterization of bone using nanoindentation technique and its applications. *Eng. Sci.* **22**, 820 (2023). <https://doi.org/10.30919/es8d820>
57. B. Li, N. Wu, Y. Yang, F. Pan, C. Wang et al., Graphene oxide-assisted multiple cross-linking of MXene for large-area, high-strength, oxidation-resistant, and multifunctional films. *Adv. Funct. Mater.* **33**, 2213357 (2023). <https://doi.org/10.1002/adfm.202213357>
58. H. Cheng, Z. Lu, Q. Gao, Y. Zuo, X. Liu et al., PVDF-Ni/PE-CNTs composite foams with co-continuous structure for electromagnetic interference shielding and photo-electro-thermal properties. *Eng. Sci.* **16**, 331–340 (2021). <https://doi.org/10.30919/es8d518>
59. D. Zhang, S. Liang, J. Chai, T. Liu, X. Yang et al., Highly effective shielding of electromagnetic waves in MoS₂ nanosheets synthesized by a hydrothermal method. *J. Phys. Chem. Solids* **134**, 77–82 (2019). <https://doi.org/10.1016/j.jpcs.2019.05.041>
60. P. Wang, L. Yang, J. Ling, J. Song, T. Song et al., Frontal ring-opening metathesis polymerized polydicyclopentadiene carbon nanotube/graphene aerogel composites with enhanced electromagnetic interference shielding. *Adv. Compos. Hybrid Mater.* **5**, 2066–2077 (2022). <https://doi.org/10.1007/s42114-022-00543-x>

61. J. Cheng, H. Zhang, M. Ning, H. Raza, D. Zhang et al., Emerging materials and designs for low- and multi-band electromagnetic wave absorbers: the search for dielectric and magnetic synergy? *Adv. Funct. Mater.* **32**, 2200123 (2022). <https://doi.org/10.1002/adfm.202200123>
62. D. Zhang, H. Wang, J. Cheng, C. Han, X. Yang et al., Conductive WS₂-NS/CNTs hybrids based 3D ultra-thin mesh electromagnetic wave absorbers with excellent absorption performance. *Appl. Surf. Sci.* **528**, 147052 (2020). <https://doi.org/10.1016/j.apsusc.2020.147052>
63. C. Xiong, Q. Xiong, M. Zhao, B. Wang, L. Dai et al., Recent advances in non-biomass and biomass-based electromagnetic shielding materials. *Adv. Compos. Hybrid Mater.* **6**, 205 (2023). <https://doi.org/10.1007/s42114-023-00774-6>
64. H. Lee, S.H. Ryu, S.J. Kwon, J.R. Choi, S.B. Lee et al., Absorption-Dominant mmWave EMI shielding films with ultralow reflection using ferromagnetic resonance frequency tunable M-type ferrites. *Nano-Micro Lett.* **15**, 76 (2023). <https://doi.org/10.1007/s40820-023-01058-w>
65. H. Zhang, T. Liu, Z. Huang, J. Cheng, H. Wang et al., Engineering flexible and green electromagnetic interference shielding materials with high performance through modulating WS₂ nanosheets on carbon fibers. *J. Materiomics* **8**, 327–334 (2022). <https://doi.org/10.1016/j.jmat.2021.09.003>
66. M. Seol, U. Hwang, J. Kim, D. Eom, I.-K. Park et al., Solution printable multifunctional polymer-based composites for smart electromagnetic interference shielding with tunable frequency and on–off selectivities. *Adv. Compos. Hybrid Mater.* **6**, 46 (2023). <https://doi.org/10.1007/s42114-022-00609-w>
67. K. Ruan, X. Shi, Y. Zhang, Y. Guo, X. Zhong et al., Electric-field-induced alignment of functionalized carbon nanotubes inside thermally conductive liquid crystalline polyimide composite films. *Angew. Chem. Int. Ed.* **62**, e202309010 (2023). <https://doi.org/10.1002/anie.202309010>
68. T. Zhang, J. Xu, T. Luo, Extremely high thermal conductivity of aligned polyacetylene predicted using first-principles-informed united-atom force field. *ES Energy Environ.* **16**, 67–73 (2022). <https://doi.org/10.30919/eesee8c719>
69. Q. Xu, Z. Wu, W. Zhao, M. He, N. Guo et al., Strategies in the preparation of conductive polyvinyl alcohol hydrogels for applications in flexible strain sensors, flexible supercapacitors, and triboelectric nanogenerator sensors: an overview. *Adv. Compos. Hybrid Mater.* **6**, 203 (2023). <https://doi.org/10.1007/s42114-023-00783-5>
70. J. Cheng, H. Zhang, H. Wang, Z. Huang, H. Raza et al., Tailoring self-polarization of bimetallic organic frameworks with multiple polar units toward high-performance consecutive multi-band electromagnetic wave absorption at gigahertz. *Adv. Funct. Mater.* **32**, 2201129 (2022). <https://doi.org/10.1002/adfm.202201129>
71. D. Skoda, J. Vilcakova, R.S. Yadav, B. Hanulikova, T. Capkova et al., Nickel nanoparticle–decorated reduced graphene oxide via one-step microwave-assisted synthesis and its lightweight and flexible composite with Polystyrene-block-poly(ethylene-ran-butylene)-block-polystyrene polymer for electromagnetic wave shielding application. *Adv. Compos. Hybrid Mater.* **6**, 113 (2023). <https://doi.org/10.1007/s42114-023-00692-7>
72. X. Zhang, Q. Tian, B. Wang, N. Wu, C. Han et al., Flexible porous SiZrOC ultrafine fibers for high-temperature thermal insulation. *Mater. Lett.* **299**, 130131 (2021). <https://doi.org/10.1016/j.matlet.2021.130131>
73. X. Zhong, M. He, C. Zhang, Y. Guo, J. Hu et al., Heterostructured BN@Co-C@C endowing polyester composites excellent thermal conductivity and microwave absorption at C band. *Adv. Funct. Mater.* (2024). <https://doi.org/10.1002/adfm.202313544>

